

Article

L-Asparagine Assisted Synthesis of Pt/CeO₂ Nanospheres for Toluene Combustion

Yu Hao, Shaohua Chen, Xueyin Zhang and Tiehong Chen *

Smart Sensing Interdisciplinary Science Center, Key Laboratory of Advanced Energy Materials Chemistry (MOE), Institute of New Catalytic Materials Science, School of Materials Science and Engineering, Nankai University, Tianjin 300350, China

* Correspondence: chenth@nankai.edu.cn

Abstract: Pt₁/CeO₂ nanospheres (Pt/CeO₂-NS) were synthesized by the bath oiling method with L-asparagine as a necessary additive. Owing to the morphology control effect and coordination interaction of L-asparagine, CeO₂ nanospheres can retain their nanosphere structure and show stronger electronic metal-support interaction with highly dispersed Pt. Moreover, the toluene catalytic combustion performance of Pt/CeO₂-NS was investigated. The structure-performance relationship is analyzed according to the coordination state of Pt. The Pt/CeO₂-NS catalyst exhibited superior catalytic activity than the commercial CeO₂-supported Pt catalyst, which is attributed to its higher oxygen vacancy and Pt⁴⁺.

Keywords: toluene; catalytic combustion; highly dispersed Pt; L-asparagine; ceria



Citation: Hao, Y.; Chen, S.; Zhang, X.; Chen, T. L-Asparagine Assisted Synthesis of Pt/CeO₂ Nanospheres for Toluene Combustion. *Catalysts* **2022**, *12*, 887. <https://doi.org/10.3390/catal12080887>

Academic Editors: Vitali A. Grinberg and Alexander D. Modestov

Received: 16 July 2022

Accepted: 11 August 2022

Published: 12 August 2022

Publisher's Note: MDPI stays neutral with regard to jurisdictional claims in published maps and institutional affiliations.



Copyright: © 2022 by the authors. Licensee MDPI, Basel, Switzerland. This article is an open access article distributed under the terms and conditions of the Creative Commons Attribution (CC BY) license (<https://creativecommons.org/licenses/by/4.0/>).

1. Introduction

Volatile organic compounds (VOCs), threats to human health, are the main precursors of surface ozone and photochemical smog, and can cause sensory stimulation, allergy, and acute or chronic respiratory diseases [1–3]. At present, catalytic combustion is considered an effective method to eliminate VOCs due to its relatively low ignition temperature, high VOC treatment capacity, and desirable selectivity to non-toxic products [4]. Among catalytic combustion catalysts, Pt-based catalysts show excellent performance and receive much attention [5–7].

Cerium dioxide (CeO₂) has been widely used in selective catalytic reduction of NO_x by NH₃ (NH₃-SCR) [8], CO oxidation [9], and catalytic combustion of volatile organic compounds (VOCs) [10–12] due to its excellent oxidation-reduction performance and high oxygen storage/release capacity. In addition, CeO₂ can anchor noble metals and promote noble metal dispersion. The interaction strength between CeO₂ and noble metals affects the catalytic activity and reaction mechanism. Peng et al. studied the size effect of Pt nanoparticles on CeO₂ for toluene oxidation. Results showed that the structure and chemical properties of Pt/CeO₂ largely depended on the particle size of Pt. Pt-O-Ce bonds, Ce³⁺, and oxygen vacancies increased with the increase in particle size. Pt/CeO₂-1.8 with a Pt particle size of 1.8 nm showed the best catalytic performance due to the balance between Pt dispersion and CeO₂ oxygen vacancy concentration [13]. The shape and size of CeO₂ also significantly affect the catalytic activity of toluene oxidation [14]. Peng et al. synthesized Pt/CeO₂ with CeO₂ nanorods, nanoparticles, and nanocubes as supports and studied their toluene oxidation performance. The results showed that Pt loaded on nanorods (Pt/CeO₂-r) showed the best catalytic activity due to its best reducibility and highest surface oxygen vacancy concentration. Moreover, preparation methods also affect activity and stability. Lee et al., designed a post-encapsulated composite structure in which individual Pt nanoparticles were encapsulated by the gas permeable and catalytically active CeO₂ shell. The Ce precursor complex with a negative charge was spontaneously adsorbed by the positively charged surfactant on the surface of a Pt nanoparticle and then restricted to

precipitation to form CeO_2 . The enhanced metal-support interaction significantly prevented Pt aggregation, resulting in high activity for methane combustion [15].

The noble metal single-atom catalysts have received widespread attention due to their excellent catalytic activity and low economic costs. However, under high temperature conditions, single atoms tend to aggregate into clusters or nanoparticles, which reduces the catalytic activity [16]. The chemical interaction between the metal atoms and the support surface can be constructed by strong coordinative interactions or surface lattice reconstruction, which makes it more likely to obtain thermally stable single atom catalysts. It is necessary to rationally design the coordination structure of metal atoms [17,18].

Amino acids with desirable functional groups (such as $-\text{NH}_2$, $-\text{SH}$, $-\text{COOH}$, and $-\text{OH}$) can strongly coordinate with noble metal ions. Complexes formed by amino acids with noble metal ions can significantly regulate the reduction of noble metals and control their structure and morphology. Shao et al. synthesized nano-gold with L- aspartic acid. It is obvious that L-aspartic acid has the ability to prepare gold nanosheets, mainly due to its specific adsorption [19].

Based on the hydrolysis of cerium nitrate and coordination between amino acids and noble metals, CeO_2 nanospheres ($\text{CeO}_2\text{-NS}$) and Pt/ CeO_2 nanospheres (Pt/ $\text{CeO}_2\text{-NS}$) with highly dispersed Pt were prepared. The reaction mechanism and effect of L-asparagine were studied systematically. Moreover, Pt/ $\text{CeO}_2\text{-NS}$ was used for toluene catalytic combustion and showed higher activity than Pt/ CeO_2 . The differences in their performance were explored based on the structure characterization.

2. Results and Discussion

2.1. Characterization of Material Structure

Figure 1 shows the XRD patterns of $\text{CeO}_2\text{-NS}$ before calcination, Pt/ $\text{CeO}_2\text{-NS}$ before calcination, $\text{CeO}_2\text{-NS}$, and Pt/ $\text{CeO}_2\text{-NS}$. Their XRD characteristic peaks are consistent with the standard card of face-centered cubic CeO_2 (JCPDS NO.43-1002). The Pt loading of Pt/ $\text{CeO}_2\text{-NS}$ determined by ICP-AES is 1.14 wt%, which is close to the theoretical loading of 1 wt%. No diffraction peak corresponding to Pt (JCPDS NO.04-0802) arises in these samples, which indicates that Pt is highly dispersed [20].

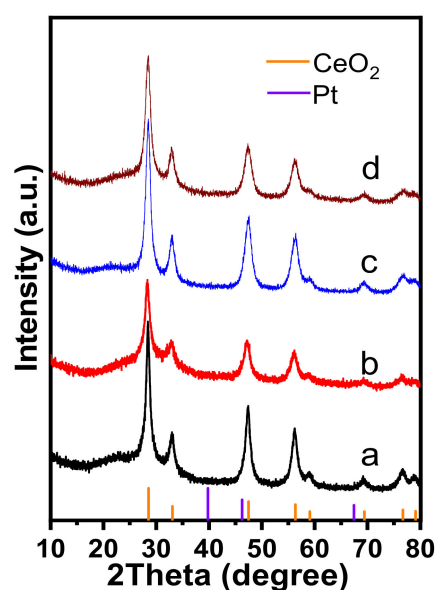


Figure 1. XRD patterns of (a) $\text{CeO}_2\text{-NS}$ before calcination; (b) Pt/ $\text{CeO}_2\text{-NS}$ before calcination; (c) $\text{CeO}_2\text{-NS}$ and (d) Pt/ $\text{CeO}_2\text{-NS}$.

Figure 2 shows SEM images of $\text{CeO}_2\text{-NS}$ before calcination, Pt/ $\text{CeO}_2\text{-NS}$ before calcination, $\text{CeO}_2\text{-NS}$, and Pt/ $\text{CeO}_2\text{-NS}$. Their nanosphere structure can be maintained to

some extent even after calcination. According to XRD and SEM, these samples have no significant change in phase structure and morphology before and after calcination.

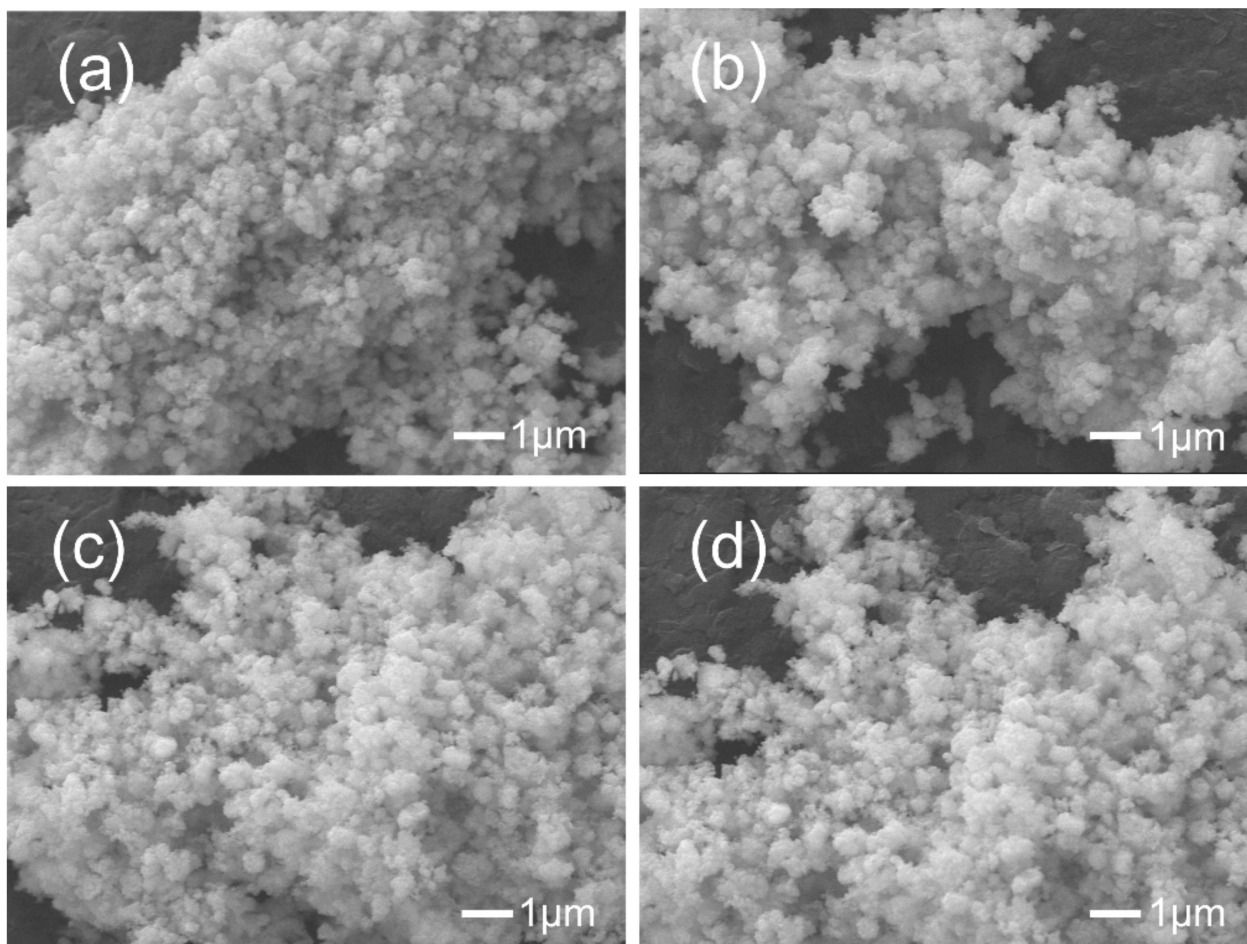


Figure 2. SEM images of (a) CeO₂-NS before calcination; (b) Pt/CeO₂-NS before calcination; (c) CeO₂-NS and (d) Pt/CeO₂-NS.

Figure 3 shows nitrogen adsorption-desorption isotherms and pore size distribution curves of CeO₂-NS and Pt/CeO₂-NS. The two samples show I-IV composite adsorption-desorption isotherms (Figure 3A) with micropores of about 1.5 nm and stacked secondary pores of 10–100 nm (Figure 3B). The specific surface area, pore size distribution, and pore volume of CeO₂-NS and Pt/CeO₂-NS are listed in Table 1. Loading of Pt showed a negligible influence on the pore structure.

Table 1. Specific surface area, pore size, and pore volume of CeO₂-NS and Pt/CeO₂-NS.

Sample	BET Surface Area (m ² /g)	Micropore Size (nm)	Secondary Pore Size (nm)	Pore Volume (cm ³ /g)
CeO ₂ -NS	75	~1.5	10–100	0.10
Pt/CeO ₂ -NS	70	~1.5	10–100	0.11

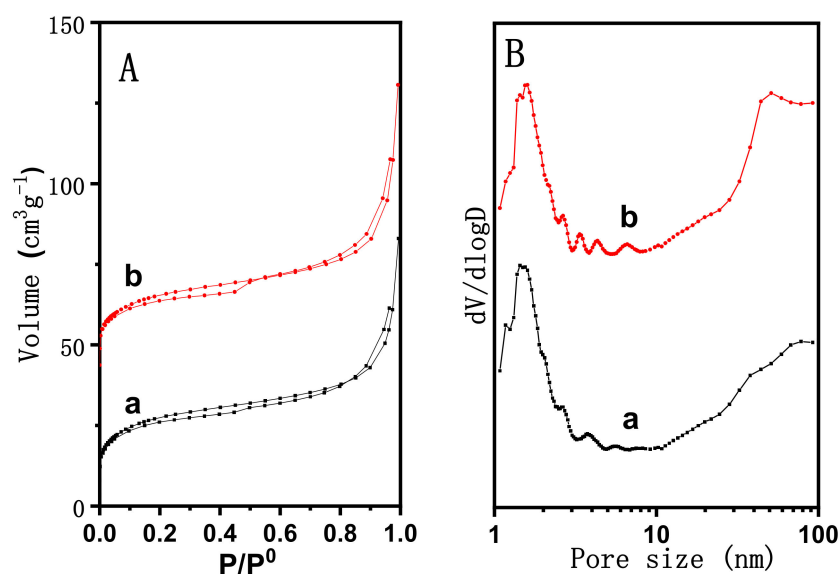


Figure 3. (A) Nitrogen adsorption-desorption isotherms and (B) pore size distribution curves of (a) CeO₂-NS and (b) Pt/CeO₂-NS.

Figure 4 shows the TEM, HRTEM, and EDS elemental mapping of CeO₂-NS and Pt/CeO₂-NS. They are all nanospheres with a particle size of about 50–200 nm (Figure 4a,d). Moreover, it can be seen from Figure 4b,e that CeO₂-NS and Pt/CeO₂-NS show a certain degree of single crystal characteristics, which shows that the orientations of the grains constituting the ceria nanospheres are correlated rather than randomly packed, and the lattice spacing is 0.31 nm, which is consistent with the face-centered cubic (111) crystal plane. This indicates that the formation of CeO₂ nanospheres conforms to the orientation adhesion mechanism [21,22]. According to Figure 4c,f, Pt is uniformly distributed in Pt/CeO₂-NS, which is consistent with XRD.

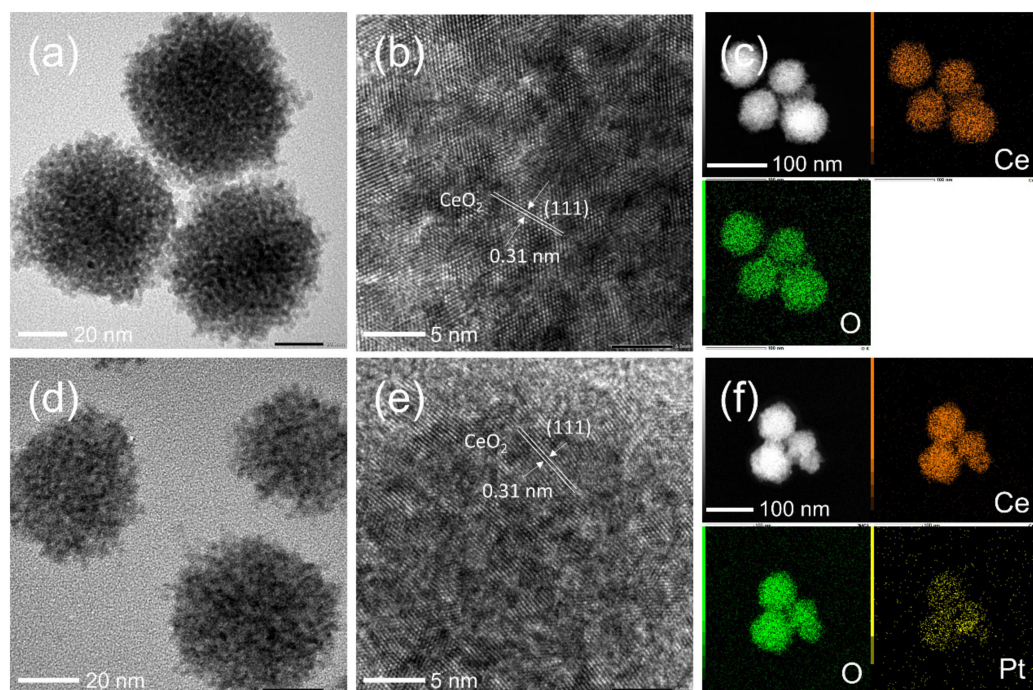


Figure 4. TEM images of (a) CeO₂-NS and (d) Pt/CeO₂-NS; HRTEM images of (b) CeO₂-NS and (e) Pt/CeO₂-NS; EDS elemental mappings of (c) CeO₂-NS and (f) Pt/CeO₂-NS.

2.2. Research on Synthesis Mechanism

It has been reported that the formation of CeO₂ nanosphere goes through stages of hydrolyzation and oxidation of cerium nitrate, formation and growth of the crystal nucleus, and orientation adhesion of nanocrystallites [23–26]. To explore the effect of reaction time and calcination on CeO₂ nanosphere synthesis, the XRD patterns of CeO₂-NS synthesized by condensation reflux for 2 h, 4 h, and 6 h were compared. According to Figure 5A, the CeO₂ crystal phase had already formed within 2 h, and the CeO₂ crystal phase remained after 4 h and 6 h of reaction. It was found by weighing the product that the yield increased with the extension of time. Figure 6 shows SEM images of CeO₂-NS reaction for 2 h, 4 h, and 6 h, in which negligible morphological change can be observed. Moreover, calcination also has no obvious influence on their crystal phase and morphology.

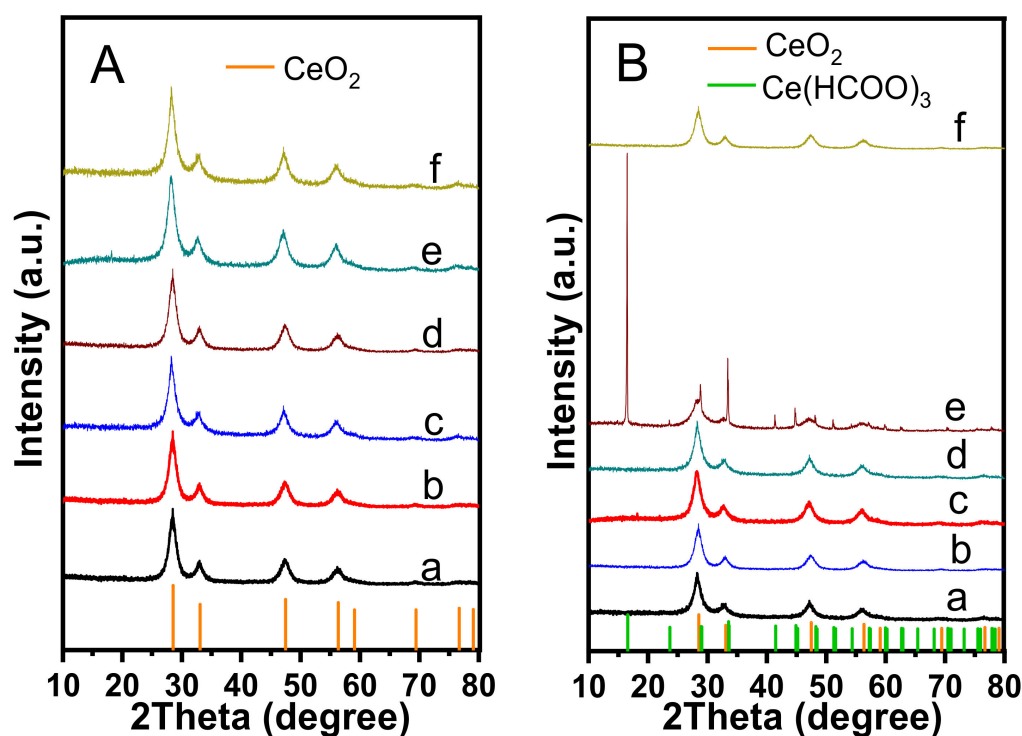


Figure 5. (A) XRD patterns of (a) CeO₂-NS 2 h before calcination; (b) CeO₂-NS 2 h; (c) CeO₂-NS 4 h before calcination; (d) CeO₂-NS 4 h; (e) CeO₂-NS before calcination and (f) CeO₂-NS; (B) XRD patterns of (a) CeO₂-NS-NA 2 h before calcination; (b) CeO₂-NS-NA 2 h; (c) CeO₂-NS-NA 4 h before calcination; (d) CeO₂-NS-NA 4 h; (e) CeO₂-NS-NA before calcination, and (f) CeO₂-NS-NA.

In order to explore the effect of L-asparagine, CeO₂-NS-NA and Pt/CeO₂-NS-NA were synthesized without L-asparagine. According to Figure 5B, when the reaction time was 6 h, in addition to CeO₂, cerium formate (JCPDS NO.49-1245) appeared before calcination, which was because part of the solvent polyethylene glycol was oxidized to oxalic acid (HOOC-COOH) under the oxidation of CeO₂, and then oxidized to formic acid (HCOOH). While the polyethylene glycol was gradually oxidized, the Ce⁴⁺ was gradually reduced to Ce³⁺, and then Ce³⁺ reacted with HCOOH to form cerium formate Ce(HCOO)₃ [27]. According to Figure 7a–d, CeO₂-NS-NA synthesized at 2 h and 4 h are still nanospheres. However, in Figure 7e–f, CeO₂-NS-NA synthesized at 6 h shows conical morphology before and after calcination. The results implied that a Ce(HCOO)₃ cone might form without L-asparagine.

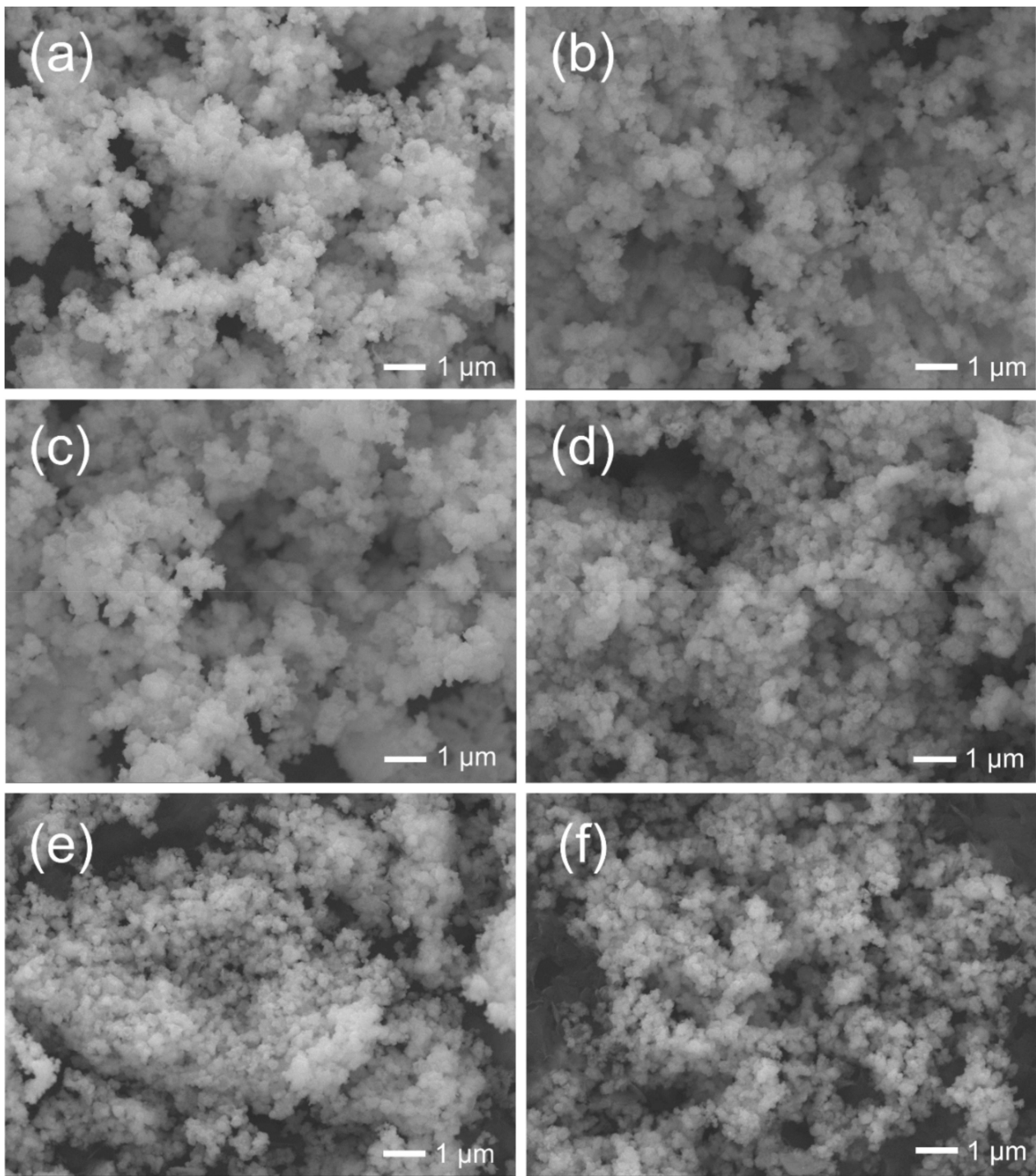


Figure 6. SEM images of (a) CeO₂-NS 2 h before calcination; (b) CeO₂-NS 2 h; (c) CeO₂-NS 4 h before calcination; (d) CeO₂-NS 4 h; (e) CeO₂-NS before calcination, and (f) CeO₂-NS.

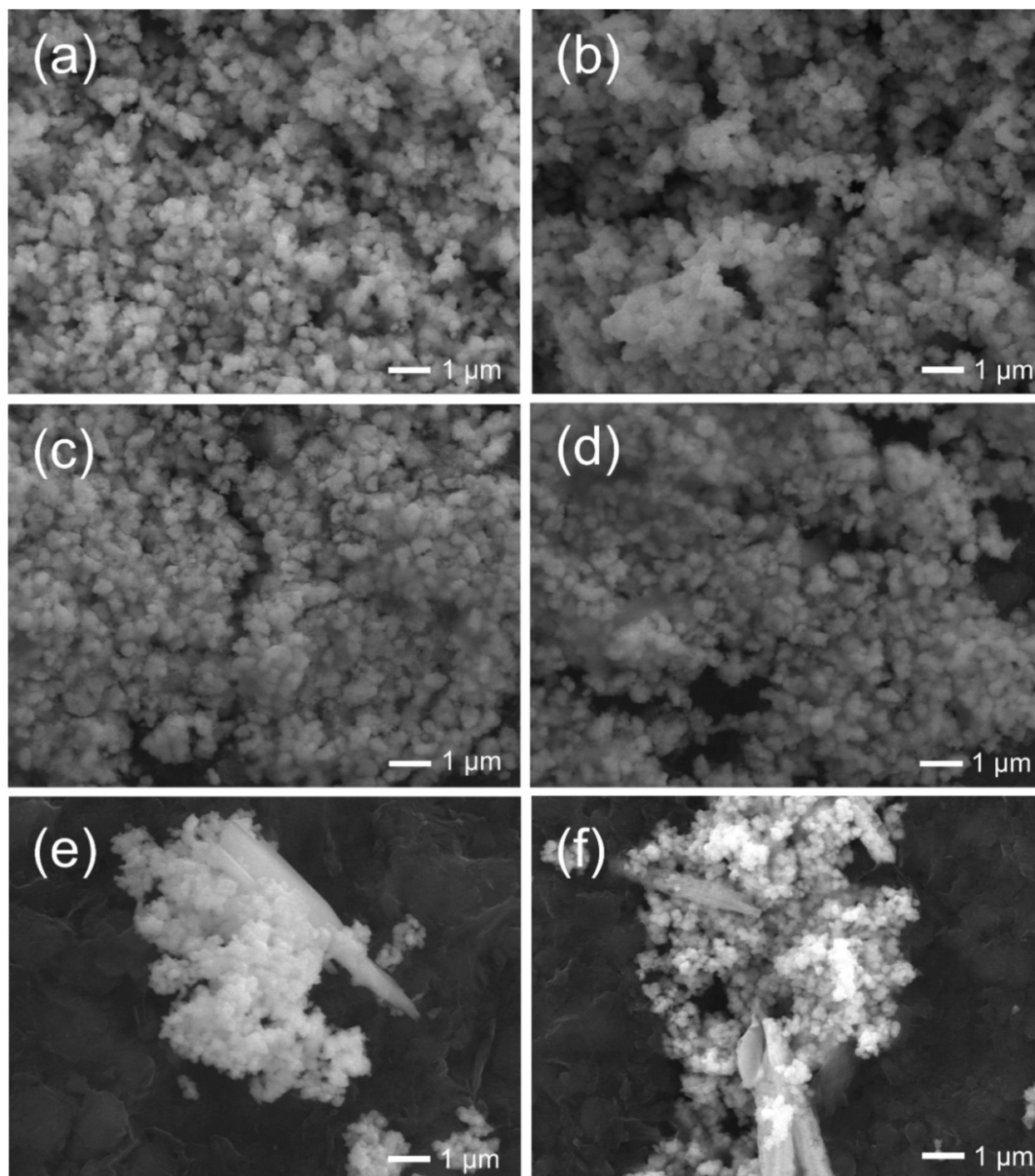


Figure 7. SEM images of (a) CeO₂-NS-NA 2 h before calcination; (b) CeO₂-NS-NA 2 h; (c) CeO₂-NS-NA 4 h before calcination; (d) CeO₂-NS-NA 4 h (e) CeO₂-NS-NA before calcination, and (f) CeO₂-NS-NA.

The XRD pattern of Pt/CeO₂-NS-NA (Figure 8) shows three distinct diffraction peaks (2θ at 39.8°, 46.2°, and 67.5°) corresponding to Pt (JCPDS NO.04-0802) [28,29]. Without L-asparagine, only nanoparticles encapsulated by some amorphous substance can be obtained (Figure 9a–c). According to EDS (Figure 9d), these nanoparticles are mainly Pt, while the content of Ce and O is very low, which indicates that chloroplatinic acid may hinder cerium nitrate hydrolyzation. In summary, L-asparagine can prevent the formation of by-product cerium formate and plays an essential role in the in situ loading of Pt.

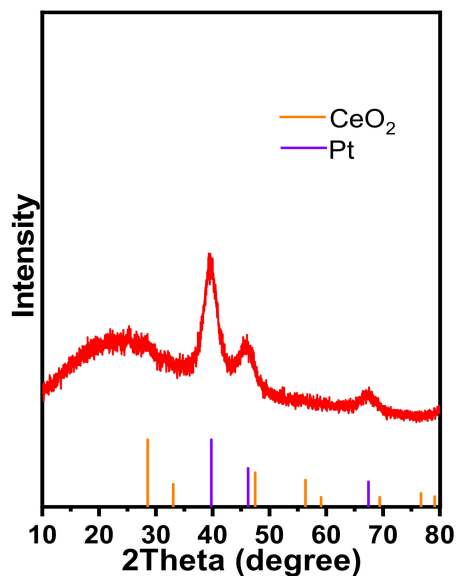


Figure 8. XRD pattern of Pt/CeO₂-NS-NA.

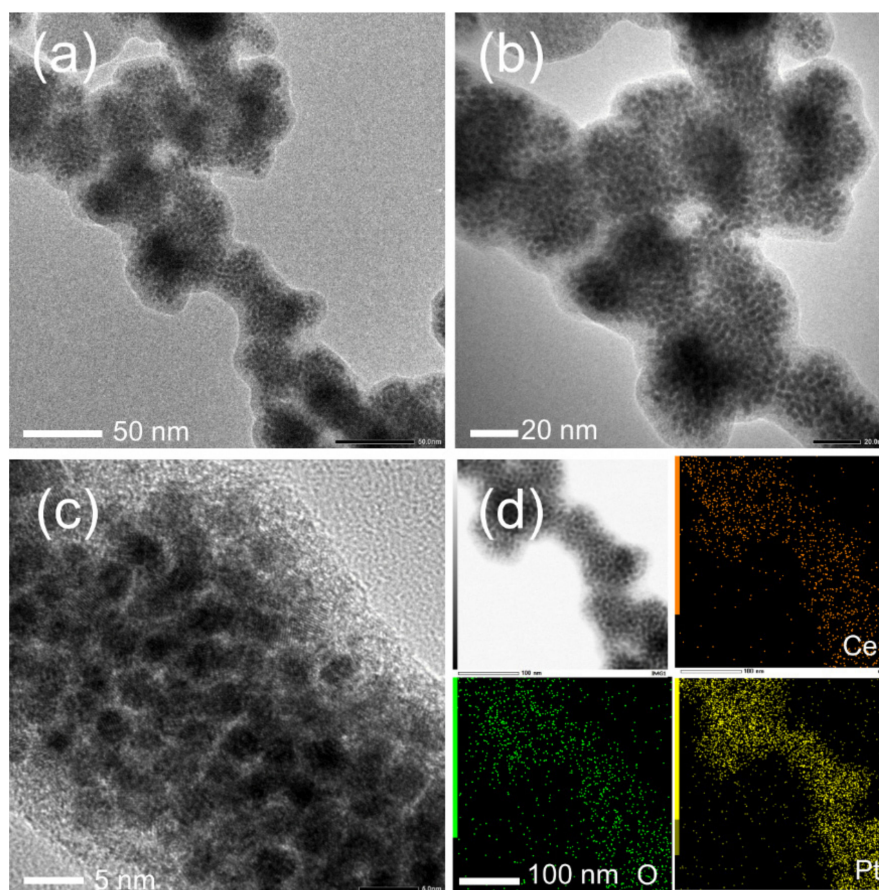


Figure 9. (a–c) TEM, and (d) EDS element mapping of the Pt/CeO₂-NS-NA.

2.3. Toluene Catalytic Combustion Activity

Pt/CeO₂ was prepared by impregnation with commercial CeO₂ as the support. The actual Pt loading amount of Pt/CeO₂ is 1.16 wt% measured by ICP, which is similar to that of Pt/CeO₂-NS and close to the theoretical loading of 1 wt%. Figure 10 and Table 2 show the toluene catalytic combustion activities of Pt/CeO₂-NS and Pt/CeO₂. Pt/CeO₂-NS shows

much better performance than that of Pt/CeO₂. Figure 10B and Table 2 show T₅₀ (reaction temperature at 50% conversion) and T₉₀ (reaction temperature at 90% conversion) of the two catalysts. Pt/CeO₂-NS has T₅₀ and T₉₀ of 224 °C and 237 °C, respectively, whereas Pt/CeO₂ has T₅₀ and T₉₀ of 283 °C and 304 °C, respectively.

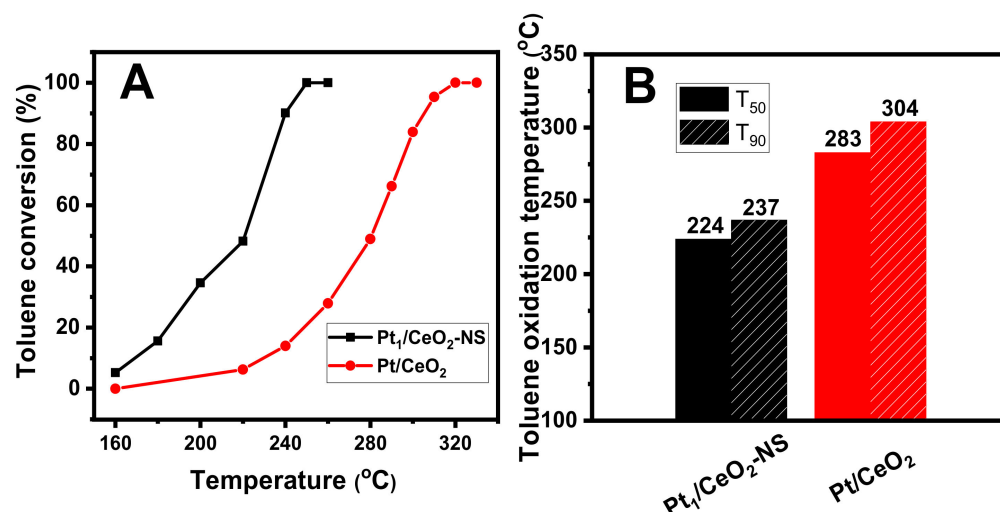


Figure 10. (A) Toluene catalytic combustion activity of Pt/CeO₂-NS and Pt/CeO₂; (B) T₅₀ and T₉₀ of Pt/CeO₂-NS and Pt/CeO₂.

Table 2. Pt loading amount, T₅₀ and T₉₀ of Pt/CeO₂-NS and Pt/CeO₂.

Catalyst	Pt Loading Amount (wt%)	T ₅₀ (°C)	T ₉₀ (°C)
Pt/CeO ₂ -NS	1.14	224	237
Pt/CeO ₂	1.16	283	304

Figure 11 shows the XRD pattern of Pt/CeO₂ synthesized by the impregnation method. The diffraction peak of Pt/CeO₂ is consistent with the standard card of face-centered cubic CeO₂ (JCPDS NO.43-1002). No peak corresponding to Pt arises, which is due to the high dispersion of Pt [30–32].

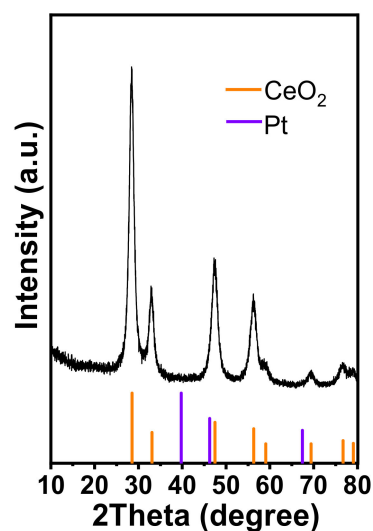


Figure 11. XRD pattern of Pt/CeO₂.

Figure 12 shows O 1s, Pt 4f, and Ce 3d XPS spectra of Pt/CeO₂-NS and Pt/CeO₂. In the O 1s spectrum, peaks at about 529.5 eV, 531.7 eV, and 533.6 eV belong to lattice oxygen species (O_{latt}: O²⁻), surface adsorbed oxygen species (O_{ads}: O²⁻, O₂²⁻, or O⁻), and physically adsorbed water (O_{H₂O}), respectively. As can be seen from Table 3, the surface oxygen ratio of Pt/CeO₂-NS is much higher than that of Pt/CeO₂, which can be attributed to more oxygen vacancy on Pt/CeO₂-NS. Figure 12B shows the Pt 4f spectrum. Peaks at about 72.8 eV and 74.6 eV correspond to the 4f_{7/2} peak of Pt²⁺ and the 4f_{7/2} peak of Pt⁴⁺, respectively. The ratio of Pt²⁺/Pt²⁺+Pt⁴⁺ is shown in Table 3. As can be seen from Figure 12B and Table 3, Pt existed in the form of Pt²⁺ and Pt⁴⁺ in Pt/CeO₂-NS and Pt/CeO₂ catalysts, and there was no Pt⁰. Pt/CeO₂-NS has more Pt⁴⁺ than Pt/CeO₂, which is more conducive to toluene catalytic combustion [33,34]. Figure 12C shows the Ce 3d spectrum, u''' (916.9), v''' (898.6), u'' (907.7), v'' (889.9), u (901.1), and v (882.7) correspond to Ce⁴⁺, and u' (903.7), v' (885.8), u₀ (898.4), and v₀ (880.8) correspond to Ce³⁺ [35]. The ratio of Ce³⁺/Ce³⁺+Ce⁴⁺ calculated quantitatively is listed in Table 3. The Ce³⁺ ratio of Pt/CeO₂-NS is higher than that of Pt/CeO₂, which is consistent with the O 1s spectrum.

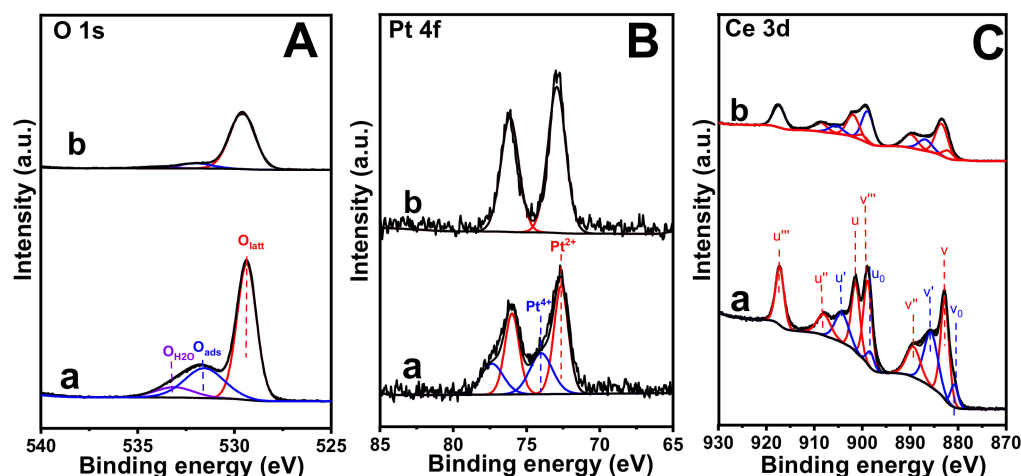


Figure 12. (A) O 1s; (B) Pt 4f and (C) Ce 3d XPS spectra of (a) Pt/CeO₂-NS and (b) Pt/CeO₂.

Table 3. Ratios of O_{ads}/O_{latt}+O_{ads}+O_{H₂O}, Pt⁴⁺/Pt²⁺+Pt⁴⁺, and Ce³⁺/Ce³⁺+Ce⁴⁺ of Pt/CeO₂-NS and Pt/CeO₂ measured by XPS.

Catalyst	O _{ads} /O _{latt} +O _{ads} +O _{H₂O}	Pt ⁴⁺ /Pt ²⁺ +Pt ⁴⁺	Ce ³⁺ /Ce ³⁺ +Ce ⁴⁺
Pt/CeO ₂ -NS	0.28	0.39	0.30
Pt/CeO ₂	0.11	—	0.20

X-ray absorption spectroscopy (XAS) was used to analyze the coordination structure and valence of Pt in Pt/CeO₂-NS. Pt foil and PtO₂ were used as the reference samples. Figure 13A shows the Pt L₃-edge XANES spectra. It can be seen that the white line strength of Pt/CeO₂-NS is similar to that of PtO₂ rather than Pt foil, which indicates that the valence state of Pt is close to +4, which is consistent with the Pt 4f XPS results. According to Pt L₃-edge EXAFS data in R space (Figure 13B), the first peak in 1–2 Å is attributed to the coordination of Pt-O [31,36]. The peak of Pt/CeO₂-NS in 2–3 Å (Pt-O-Pt) is different from that of PtO₂, which indicates that there is undetectable coordination of Pt-O-Pt related to PtO₂. At the same time, the XPS (Figure 12) results show that there is no Pt⁰ in the Pt/CeO₂-NS catalyst, which indicates that the Pt is highly dispersed in the Pt/CeO₂-NS [37]. The Pt-O-Ce structure is used to fit the first and second coordination layers. The EXAFS fitting curve and fitting parameters are shown in Figure 13C and Table 4. These results demonstrate that the highly dispersed Pt exists in the form of Pt-O-Ce in the Pt/CeO₂-NS catalyst.

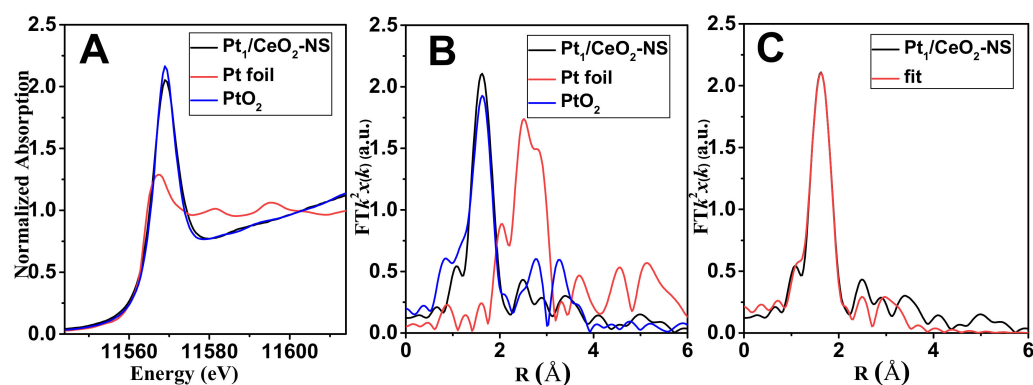


Figure 13. (A) Pt L₃-edge XANES spectra and (B) R-space spectra from Pt L₃-edge EXAFS data of Pt/CeO₂-NS, Pt foil, and PtO₂; (C) Corresponding EXAFS fitting curve of Pt/CeO₂-NS.

Table 4. EXAFS fitting parameters at Pt L₃-edge for Pt/CeO₂-NS.

Sample	Shell	CN ^a	R (Å) ^b	σ ² ^c	ΔE ₀ ^d	R Factor
Pt/CeO ₂ -NS	Pt-O	5.2 ± 0.3	2.00 ± 0.01	0.0017	11.0 ± 1.7	0.0132
	Pt-O1	1.4 ± 0.6	2.45 ± 0.03	0.0016		
	Pt-O-Ce	2.0 ± 1.4	3.20 ± 0.04	0.0071		

^a CN: coordination numbers; ^b R: bond distance; ^c σ²: Debye–Waller factors; ^d ΔE₀: edge correction.

From the activity of toluene catalytic combustion, it can be seen that the catalytic performance of the Pt/CeO₂-NS catalyst is better than that of the Pt/CeO₂ catalyst. From the characterization results of XRD, ICP, XPS, and XAS, it can be seen that the Pt loadings of the Pt/CeO₂-NS catalyst and the Pt/CeO₂ catalyst are similar, and both catalysts have no obvious Pt nanoparticles, but the Pt/CeO₂-NS has more oxygen vacancies and Pt⁴⁺, which are more favorable for the catalytic reaction.

3. Experimental Section

3.1. Materials

L-asparagine (C₄H₈N₂O₃), cerium nitrate hexahydrate (Ce(NO₃)₃·6H₂O), polyethylene glycol 400, chloroplatinic acid hexahydrate (H₂PtCl₆·6H₂O), commercial CeO₂, orthoboric acid (H₃BO₃), nitric acid (HNO₃), and hydrofluoric acid (HF) were purchased from Aladdin (Shanghai, China). Hydrochloric acid (HCl) was purchased from Chemical Reagent Wholesale Company (Tianjin, China).

3.2. Catalyst Preparation

One mmol of L-asparagine was dissolved in 4 g of water at 45 °C. Under strong stirring, 2 mmol of cerium nitrate was added to the above solution. After all the cerium nitrate had dissolved, 80 g of polyethylene glycol 400 was added. After stirring for 10 min, the obtained solution was transferred into a 100 mL round bottom-flask and condensed by reflux in an oil bath at 160 °C for 6 h. The product was washed with deionized water and absolute ethanol, dried at 60 °C, and then calcined at 360 °C for 1 h at a rate of 5 °C/min in a muffle furnace under static air. The sample was named CeO₂-NS. The samples synthesized by condensation reflux reaction for 2 h and 4 h were designated as CeO₂-NS-2 h and CeO₂-NS-4 h, respectively.

One mmol of L-asparagine was dissolved in 4 g of water at 45 °C. Under strong stirring, 2 mmol of cerium nitrate was added to the above-mentioned L-asparagine aqueous solution, then 9.0 mg of chloroplatinic acid hexahydrate was added, and then 80 g of polyethylene glycol 400 was added. After stirring for 10 min, the obtained solution was transferred into a round-bottom flask (100 mL), condensed by reflux in an oil bath at 160 °C for 6 h, washed with deionized water and absolute ethanol, dried at 60 °C and calcined at 400 °C for 2 h at

the rate of 5 °C/min in a muffle furnace (Tianjin Central Electric Furnace Co., Ltd., Tianjin, China) under static air. The sample was named Pt/CeO₂-NS. The loading of Pt was 1 wt%.

The samples synthesized without L-asparagine were used for comparison. Two mmol of cerium nitrate was dissolved in 4 g of water, and then 80 g of polyethylene glycol 400 was added. After stirring for 10 min, the solution was transferred into a 100 mL round-bottom flask, condensed by reflux in an oil bath at 160 °C for 6 h, then washed with deionized water and absolute ethanol, dried at 60 °C, and calcined at 360 °C for 1 h at a rate of 5 °C/min in a muffle furnace under static air. The sample was named CeO₂-NS-NA. The samples synthesized by condensation reflux reaction for 2 h and 4 h were named CeO₂-NS-NA-2 h and CeO₂-NS-NA-4 h, respectively. Then, 2 mmol of cerium nitrate was dissolved in 4 g of water, then 9.0 mg of chloroplatinic acid hexahydrate was added, and then 80 g of polyethylene glycol 400 was added. After stirring for 10 min, the solution was transferred into a 100 mL round-bottom flask, condensed by reflux in an oil bath at 160 °C for 6 h, washed with deionized water and absolute ethanol, dried at 60 °C, and calcined at 360 °C for 1 h at a rate of 5 °C/min in a muffle furnace under static air. The sample was denoted as Pt/CeO₂-NS-NA.

0.3 g of commercial CeO₂ was dispersed in 6 mL of ethanol. After stirring for 0.5 h, 8.0 mg of chloroplatinic acid hexahydrate was added. After being stirred for 0.5 h, heated to evaporate and dried at 80 °C, the product was calcined in a muffle furnace at 400 °C for 2 h at a rate of 5 °C/min in a muffle furnace under static air. The sample was denoted as Pt/CeO₂.

3.3. Characterization

X-ray diffraction (XRD) was tested on the Rigaku Smart Lab 3kW diffractometer (Rigaku Corporation, Japan) (Cu K_α) with a tube voltage of 40 kV and a tube current of 40 mA.

The morphology of the samples was measured by field emission scanning electron microscopy (FE-SEM, JSM-7800, JEOL, Tokyo, Japan).

The high-resolution morphology and element distribution of the samples were measured by transmission electron microscopy (TEM, JEM-2800, JEOL, Japan) with an energy dispersive spectrometer (EDS). Before the measurement, all samples were ultrasonically dispersed in ethanol and then dropped onto the carbon film.

The elemental composition and valence of the sample surface were determined by X-ray photoelectron spectroscopy (XPS, Thermo Scientific ESCALAB 250Xi, Thermo, Waltham, MA, USA) with an Al K_α X-ray source, and the C 1s peak (BE = 284.8 eV) was used for calibration.

The Pt loading amount was measured by inductively coupled plasma atomic emission spectrometry (ICP-AES, SpectroBlue, Spectro Analytical Instruments, Kleve, Germany). A certain amount of sample was added to the sample tube, then a certain amount of aqua regia and HF were added in turn and heated to dissolve. After dissolution, the solution was poured into a volumetric flask. The remaining solution was washed several times with deionized water and added to the volumetric flask. Then a certain amount of 4% H₃BO₃ was added, and finally the volume is fixed in the volumetric flask.

The specific surface area, pore volume, and pore size of the samples were measured by the micromeritics ASAP 2020 physical adsorption instrument (Micromeritics, Norcross, GA, USA). N₂ adsorption and desorption isotherms were measured at liquid nitrogen temperature. The BET (Brunauer-Emmett-Teller) method was used to calculate the specific surface area, and the BJH (Barrett-Joynew-Halenda) method was used to calculate the pore size distribution and pore volume.

The X-ray absorption fine structure spectra (XAFS) Pt L₃-edge were collected at the BL07A1 beamline of the National Synchrotron Radiation Research Center (NSRRC). The data were collected using a Lytle detector in fluorescence mode, while the corresponding reference sample was collected in transmission mode.

3.4. Catalytic Combustion of Toluene

The catalytic oxidation of toluene was carried out in the fixed bed reactor (WFS-2017, Tianjin Xianquan Industry and Trade Development Co. LTD, Tianjin, China). A quantity of 0.1 g of the catalyst with a particle size of 40–60 mesh was placed in the middle of the tubular reactor and fixed by quartz cotton. The temperature of the catalyst was monitored by a thermocouple placed in the middle of the reaction bed. Before testing, the catalyst was heated under N₂ gas (50 mL/min) at 200 °C for 1 h. Synthetic air (21% O₂ + 79% N₂) was bubbled into the carrier gas tank containing pure toluene and then diluted with another stream of air before reaching the reaction bed to obtain a mixture inlet gas of 1000 ppm toluene. In order to stabilize the saturated vapor pressure of toluene, a condensate pump was used to control the temperature of the tank containing toluene. The total flow rate was maintained at 100 mL/min, corresponding to the weight hourly space velocity (GHSV) of 60,000 mL·g⁻¹·h⁻¹.

The concentrations of toluene, carbon dioxide, and by-products were analyzed by the SP-7890 gas chromatograph (Shandong Lunan Ruihong Chemical Instruments Co., Ltd., Shandong, China) equipped with two flame ionization detectors (FID), one equipped with a methanation furnace for CO and CO₂ detection, and the other for toluene and organic by-products such as benzene. The channel for organics was adopted as a SE-30 capillary column (30 m × 0.32 mm × 0.25 μm). The concentrations of CO and CO₂ were measured by a TDX-01 column. The formation of benzene was not observed in our whole set of experiments. A negligible amount of CO was observed at low temperature, and it disappeared completely when the temperature increased, which can be proved by the carbon contents in the inlet and outlet gases based on toluene and CO₂. Such a small amount of the by-products has little effect on toluene conversion. The conversion of toluene was calculated by the following Formula (1):

$$\text{Toluene Conversion (\%)} = \frac{C_{\text{Tol,in}} - C_{\text{Tol,out}}}{C_{\text{Tol,in}}} \times 100\% \quad (1)$$

4. Conclusions

In summary, porous CeO₂ nanospheres with highly dispersed Pt were synthesized via an L-asparagine assisted bath oiling method. L-asparagine, as an additive, could inhibit the formation of cerium formate and coordinate with Pt. For toluene catalytic combustion, Pt/CeO₂-NS showed much better catalytic activity than Pt/CeO₂ synthesized by impregnation with commercial CeO₂ as the support, which could be attributed to more Pt⁴⁺ and oxygen vacancy on Pt/CeO₂-NS. Therefore, L-asparagine is an effective additive for preparing Pt-based toluene combustion catalysts.

Author Contributions: Conceptualization and writing-original draft preparation, Y.H.; experiments, Y.H. and S.C.; data analysis, Y.H., S.C. and X.Z.; writing-review and editing, funding acquisition and supervision, T.C. All authors have read and agreed to the published version of the manuscript.

Funding: National Natural Science Foundation of China (NO. 21773128).

Data Availability Statement: Data available upon request.

Conflicts of Interest: The authors declare that they have no known competing financial interests or personal relationships that could have appeared to influence the work reported in this paper.

References

1. Bi, F.; Zhang, X.; Chen, J.; Yang, Y.; Wang, Y. Excellent catalytic activity and water resistance of UiO-66-supported highly dispersed Pd nanoparticles for toluene catalytic oxidation. *Appl. Catal. B Environ.* **2020**, *269*, 118767. [[CrossRef](#)]
2. Chang, M.; Liu, X.; Ning, P.; Zhang, Q.; Xia, F.; Wang, H.; Wei, G.; Wen, J.; Liu, M.; Hu, J.; et al. Removal of toluene over bi-metallic Pt–Pd-SBA-15 catalysts: Kinetic and mechanistic study. *Micropor. Mesopor. Mat.* **2020**, *302*, 110111. [[CrossRef](#)]
3. Li, S.; Wang, D.; Wu, X.; Chen, Y. Recent advance on VOCs oxidation over layered double hydroxides derived mixed metal oxides. *Chinese J. Catal.* **2020**, *41*, 550–560. [[CrossRef](#)]

4. Lei, J.; Wang, S.; Li, J. Mesoporous Co₃O₄ Derived from Facile Calcination of Octahedral Co-MOFs for Toluene Catalytic Oxidation. *Ind. Eng. Chem. Res.* **2020**, *59*, 5583–5590. [[CrossRef](#)]
5. Liu, G.; Tian, Y.; Zhang, B.; Wang, L.; Zhang, X. Catalytic combustion of VOC on sandwich-structured Pt@ZSM-5 nanosheets prepared by controllable intercalation. *J. Hazard. Mater.* **2019**, *367*, 568–576. [[CrossRef](#)] [[PubMed](#)]
6. Li, Q.; Odoom-Wubah, T.; Fu, X.; Mulka, R.; Sun, D.; Zheng, Y.; Jia, L.; Huang, J.; Li, Q. Photoinduced Pt-Decorated Expanded Graphite toward Low-Temperature Benzene Catalytic Combustion. *Ind. Eng. Chem. Res.* **2020**, *59*, 11453–11461. [[CrossRef](#)]
7. Wang, Z.; Ma, P.; Zheng, K.; Wang, C.; Liu, Y.; Dai, H.; Wang, C.; Hsi, H.-C.; Deng, J. Size effect, mutual inhibition and oxidation mechanism of the catalytic removal of a toluene and acetone mixture over TiO₂ nanosheet-supported Pt nanocatalysts. *Appl. Catal. B Environ.* **2020**, *274*, 118963. [[CrossRef](#)]
8. Zhang, L.; Sun, J.; Xiong, Y.; Zeng, X.; Tang, C.; Dong, L. Catalytic performance of highly dispersed WO₃ loaded on CeO₂ in the selective catalytic reduction of NO by NH₃. *Chinese J. Catal.* **2017**, *38*, 1749–1758. [[CrossRef](#)]
9. Grabchenko, M.V.; Mamontov, G.V.; Zaikovskii, V.I.; La Parola, V.; Liotta, L.F.; Vodyankina, O.V. The role of metal-support interaction in Ag/CeO₂ catalysts for CO and soot oxidation. *Appl. Catal. B Environ.* **2020**, *260*, 118148. [[CrossRef](#)]
10. Okal, J.; Zawadzki, M.; Kraszkiewicz, P.; Adamska, K. Ru/CeO₂ catalysts for combustion of mixture of light hydrocarbons: Effect of preparation method and metal salt precursors. *Appl. Catal. A Gen.* **2018**, *549*, 161–169. [[CrossRef](#)]
11. Guo, Y.; Gao, Y.; Li, X.; Zhuang, G.; Wang, K.; Zheng, Y.; Sun, D.; Huang, J.; Li, Q. Catalytic benzene oxidation by biogenic Pd nanoparticles over 3D-ordered mesoporous CeO₂. *Chem. Eng. J.* **2019**, *362*, 41–52. [[CrossRef](#)]
12. Wang, Q.; Yeung, K.L.; Bañares, M.A. Ceria and its related materials for VOC catalytic combustion: A review. *Catal. Today* **2020**, *356*, 141–154. [[CrossRef](#)]
13. Peng, R.; Li, S.; Sun, X.; Ren, Q.; Chen, L.; Fu, M.; Wu, J.; Ye, D. Size effect of Pt nanoparticles on the catalytic oxidation of toluene over Pt/CeO₂ catalysts. *Appl. Catal. B Environ.* **2018**, *220*, 462–470. [[CrossRef](#)]
14. Peng, R.; Sun, X.; Li, S.; Chen, L.; Fu, M.; Wu, J.; Ye, D. Shape effect of Pt/CeO₂ catalysts on the catalytic oxidation of toluene. *Chem. Eng. J.* **2016**, *306*, 1234–1246. [[CrossRef](#)]
15. Lee, S.; Seo, J.; Jung, W. Sintering-resistant Pt@CeO₂ nanoparticles for high-temperature oxidation catalysis. *Nanoscale* **2016**, *8*, 10219–10228. [[CrossRef](#)]
16. Yan, D.; Chen, J.; Jia, H. Temperature-Induced Structure Reconstruction to Prepare a Thermally Stable Single-Atom Platinum Catalyst. *Angew. Chem. Int. Ed.* **2020**, *59*, 13562–13567. [[CrossRef](#)]
17. Lv, H.; Guo, W.; Chen, M.; Zhou, H.; Wu, Y. Rational construction of thermally stable single atom catalysts: From atomic structure to practical applications. *Chinese J. Catal.* **2022**, *43*, 71–91. [[CrossRef](#)]
18. Qu, Y.; Chen, B.; Li, Z.; Duan, X.; Wang, L.; Lin, Y.; Yuan, T.; Zhou, F.; Hu, Y.; Yang, Z.; et al. Thermal Emitting Strategy to Synthesize Atomically Dispersed Pt Metal Sites from Bulk Pt Metal. *J. Am. Chem. Soc.* **2019**, *111*, 4505–4509. [[CrossRef](#)]
19. Shao, Y.; Jin, Y.; Dong, S. Synthesis of gold nanoplates by aspartate reduction of gold chloride. *Chem. Commun.* **2004**, 1104–1105. [[CrossRef](#)]
20. Wang, J.-G.; Zhou, H.-J.; Sun, P.-C.; Ding, D.-T.; Chen, T.-H. Hollow Carved Single-Crystal Mesoporous Silica Templated by Mesomorphous Polyelectrolyte–Surfactant Complexes. *Chem. Mater.* **2010**, *22*, 3829–3831. [[CrossRef](#)]
21. Su, Z.; Yang, W.; Wang, C.; Xiong, S.; Cao, X.; Peng, Y.; Si, W.; Weng, Y.; Xue, M.; Li, J. Roles of Oxygen Vacancies in the Bulk and Surface of CeO₂ for Toluene Catalytic Combustion. *Environ. Sci. Technol.* **2020**, *54*, 12684–12692. [[CrossRef](#)] [[PubMed](#)]
22. Carltonbird, M.; Eaimsumang, S.; Pongstabodee, S.; Boonyuen, S.; Smith, S.M.; Luengnaruemitchai, A. Effect of the exposed ceria morphology on the catalytic activity of gold/ceria catalysts for the preferential oxidation of carbon monoxide. *Chem. Eng. J.* **2018**, *344*, 545–555. [[CrossRef](#)]
23. Liang, X.; Wang, X.; Zhuang, Y.; Xu, B.; Kuang, S.; Li, Y. Formation of CeO₂-ZrO₂ solid solution nanocages with controllable structures via kirkendall effect. *J. Am. Chem. Soc.* **2008**, *130*, 2736–2737. [[CrossRef](#)] [[PubMed](#)]
24. Li, T.; Xiang, G.; Zhuang, J.; Wang, X. Enhanced catalytic performance of assembled ceria necklace nanowires by Ni doping. *Chem. Commun.* **2011**, *47*, 6060–6062. [[CrossRef](#)] [[PubMed](#)]
25. Liang, X.; Xiao, J.; Chen, B.; Li, Y. Catalytically stable and active CeO₂ mesoporous spheres. *Inorg. Chem.* **2010**, *49*, 8188–8190. [[CrossRef](#)]
26. Shen, S.; Wang, X. Controlled growth of inorganic nanocrystals: Size and surface effects of nuclei. *Chem. Commun.* **2010**, *46*, 6891–6899. [[CrossRef](#)]
27. Guo, Z.Y.; Zhu, Y.; Meng, F.F.; Du, F.L. Facile Reflux Method Synthesis, Photo-Catalyst and Electrochemical Properties of Micro-Sized Subuliform CeO₂. *Sci. Adv. Mater.* **2014**, *6*, 2688–2693. [[CrossRef](#)]
28. Jiang, Z.; He, C.; Dummer, N.F.; Shi, J.; Tian, M.; Ma, C.; Hao, Z.; Taylor, S.H.; Ma, M.; Shen, Z. Insight into the efficient oxidation of methyl-ethyl-ketone over hierarchically micro-mesostructured Pt/K-(Al)SiO₂ nanorod catalysts: Structure-activity relationships and mechanism. *Appl. Catal. B Environ.* **2018**, *226*, 220–233. [[CrossRef](#)]
29. Qiu, Y.; Li, X.; Zhang, Y.; Xie, C.; Zhou, S.; Wang, R.; Luo, S.-Z.; Jing, F.; Chu, W. Various Metals (Ce, In, La, and Fe) Promoted Pt/Sn-SBA-15 as Highly Stable Catalysts for Propane Dehydrogenation. *Ind. Eng. Chem. Res.* **2019**, *58*, 10804–10818. [[CrossRef](#)]
30. Kondratowicz, T.; Drozdek, M.; Michalik, M.; Gac, W.; Gajewska, M.; Kuśtrowski, P. Catalytic activity of Pt species variously dispersed on hollow ZrO₂ spheres in combustion of volatile organic compounds. *Appl. Surf. Sci.* **2020**, *513*, 145788. [[CrossRef](#)]
31. Chen, L.N.; Hou, K.P.; Liu, Y.S.; Qi, Z.Y.; Zheng, Q.; Lu, Y.H.; Chen, J.Y.; Chen, J.L.; Pao, C.W.; Wang, S.B.; et al. Efficient Hydrogen Production from Methanol Using a Single-Site Pt₁/CeO₂ Catalyst. *J. Am. Chem. Soc.* **2019**, *141*, 17995–17999. [[CrossRef](#)] [[PubMed](#)]

32. Wang, Z.; Yang, H.; Liu, R.; Xie, S.; Liu, Y.; Dai, H.; Huang, H.; Deng, J. Probing toluene catalytic removal mechanism over supported Pt nano- and single-atom-catalyst. *J. Hazard. Mater.* **2020**, *392*, 122258. [[CrossRef](#)] [[PubMed](#)]
33. Tang, Y.; Wang, Y.-G.; Li, J. Theoretical Investigations of Pt₁@CeO₂ Single-Atom Catalyst for CO Oxidation. *J. Phys. Chem. C* **2017**, *121*, 11281–11289. [[CrossRef](#)]
34. Ye, X.; Wang, H.; Lin, Y.; Liu, X.; Cao, L.; Gu, J.; Lu, J. Insight of the stability and activity of platinum single atoms on ceria. *Nano Res.* **2019**, *12*, 1401–1409. [[CrossRef](#)]
35. Buitrago-Sierra, R.; Serrano-Ruiz, J.C.; Rodríguez-Reinoso, F.; Sepúlveda-Escribano, A.; Dumesic, J.A. Ce promoted Pd-Nb catalysts for γ -valerolactone ring-opening and hydrogenation. *Green Chem.* **2012**, *14*, 3318–3324. [[CrossRef](#)]
36. Jiang, Z.; Jing, M.; Feng, X.; Xiong, J.; He, C.; Douthwaite, M.; Zheng, L.; Song, W.; Liu, J.; Qu, Z. Stabilizing platinum atoms on CeO₂ oxygen vacancies by metal-support interaction induced interface distortion: Mechanism and application. *Appl. Catal. B Environ.* **2020**, *278*, 119304. [[CrossRef](#)]
37. Kunwar, D.; Zhou, S.; DeLaRiva, A.; Peterson, E.J.; Xiong, H.; Pereira-Hernández, X.I.; Purdy, S.C.; Veen, R.T.; Brongersma, H.H.; Miller, J.T.; et al. Stabilizing High Metal Loadings of Thermally Stable Platinum Single Atoms on an Industrial Catalyst Support. *ACS Catal.* **2019**, *9*, 3978–3990. [[CrossRef](#)]